Thermonuclear novae explosions: Study of RS Ophiuchi with NuGrid

Vujić, Agata

UNIVERSITY OF RIJEKA

FACULTY OF PHYSICS

Agata Vujić

Thermonuclear novae explosions: Study of RS Ophiuchi with NuGrid

Bachelor thesis

Rijeka, November 2022

UNIVERSITY OF RIJEKA

FACULTY OF PHYSICS

UNDERGRADUATE STUDY PROGRAM IN PHYSICS
COURSE INFORMATICS

Bachelor thesis

Thermonuclear novae explosions: Study of RS Ophiuchi with NuGrid

Supervisors:

dr. sc. Marina Manganaro

Candidate:

Agata Vujić

Rijeka, 22.11.2022.

Contents

Abstract

This work of thesis aims to study the properties of the recurrent nova RS Ophiuchi, whose latest outburst phase was observed in August 2021. RS Ophiuchi is a binary system composed of a red giant star and a CO white dwarf (WD). These stars are close enough to have the transfer of matter from the red giant to the WD. The accretion of this matter on the surface of the WD gives rise to recurrent releases of energy by a thermonuclear runaway.

Simulations of the nova RS Ophiuchi were made with MESA (Modules for Experiments in Stellar Astrophysics) star module as a part of the NuGrid (Nucleosynthesis Grid) collaboration's collection of software tools for simulations. Two different simulations were made for the WD profile with and without convective boundary mixing.

For each WD profile, WD models for different evolutionary paths were made, resulting in WD models with different masses of the accreted shells.

For the logarithmic luminosity of the RS Ophiuchi, a value of $\log_{10} \frac{L}{L_\odot} = 1.867$, has been obtained, and comparison with the logarithmic luminosity of models in plots of constant WD Roche lobe radius brought me to the conclusion that RS Ophiuchi has a greater mass of the accreted envelope than most models. Models with logarithmic luminosity close to the one of RS Ophiuchi of both profiles have both pp-chain, and CNO cycles ignited in their accreted envelope, confirming that these models are good models of the nova RS Ophiuchi.

Keywords: RS Ophiuchi, nova, recurrent, simulations, NuGrid, nucleosynthesis, Roche lobe

1 Introduction

Many hidden properties of our Universe can be discovered from its extremes. Most extreme conditions can be found in the stars, black holes, novae, supernovae..., and for a long time, insights could only be derived from observations of such objects and events. Today, after years of progress in computational hardware and software, simulations of these objects and events can be made on personal computers and not only on supercomputers. These simulations can be used to reveal some aspects and also to deepen our understanding of the Universe.

The main purpose of this work of thesis is to run simulations of the nova RS Ophiuchi in order to investigate the properties of this nova.

A star is a self gravitating object with gravity so strong to achieve conditions in its core for nucleosynthesis to take place. Energy released in nucleosynthesis reaction is given by the reaction Q-value, which includes the sum of the masses of all reaction partners before the reaction (in the entrance channel) and the sum of masses of final nuclei (in the exit channel).

$$Q_{nuc} = B_{before} - B_{after} = \left[\left(\sum_{initial} m_{nuc}^{initial}\right) - \left(\sum_{final} m_{nuc}^{final}\right)\right] c^2$$

Released energy, in a star, counteracts gravity and keeps a star in hydrodynamic equilibrium as long as there is enough material for continuous nucleosynthesis reactions. Hydrogen burning takes place in stars first stable phase. Hydrogen burning addresses series of reactions that converts hydrogen into helium, which can happen with different paths:

1. Proton-proton chain:
   $4\,{}^1_1\mathrm{H}^+ + 2\mathrm{e}^- \longrightarrow\ {}^4_2\mathrm{He}^{2+} + 2\nu_\mathrm{e} + 26{,}73$ MeV
2. CNO cycle: if any of the nuclides ^{12}C, ^{13}C, ^{15}N, or ^{15}N are already present in the stellar plasma, a closed reaction loop can consume four protons to make a ^{4}He nucleus

The next phase of nucleosynthesis in stars is Helium burning:

1. $\alpha +\ \alpha \longrightarrow\ {}^8_4\mathrm{Be} - 0{,}09$ MeV
2. $\alpha +\ {}^8_4\mathrm{Be} \longrightarrow\ {}^{12}_6\mathrm{C} +\ 2\,\gamma +\ 7{,}37$ MeV

Heavy stars also have carbon, neon, oxygen and silicon burning phases.

If the star with mass below $8M_{\odot}$, during its lifetime, achieved conditions for ignition of helium burning, its remnant will be mostly composed of C and O and is called CO white dwarf (WD).

The recurrent nova RS Ophiuchi is a binary star system composed of a red giant star and a CO (Carbon and Oxygen) WD. These stars are close enough to have transfer of matter from the red giant to the WD. Accretion of this matter, on a surface of the WD, will give rise to recurrent releases of energy by a thermonuclear runaway.

Nuclear astrophysics simulations, in which observed parameters of a system can be used as an input to study the evolution of a star or of systems of star and their nucleosynthesis, are a great tool to investigate the properties of the nova RS Ophiuchi, which, as expected, entered one of its outbursts phases in 2021.

Here we report the results of such simulations, performed within the NuGrid international collaboration [1].

This work is organized as follows:
In Sec. 2 the various nucleosynthesis processes will be explained in detail. In Sec. 4 the evolutionary paths of the stars will be described as well. In Sec. 5 the novae will be defined by presenting their sub-categories with highlight on the nova RS Ophiuchi (Sec. 5.4).
The simulations of the nova RS Ophiuchi, will be presented in Sec. 6. A description of the software is given in Sec. 6.2. The results of the simulations, including interesting insights for properties of the accreted envelope of the WD, will be presented in Sec. 7. Sec. 8 deals with the discussion of the results, and, finally, conclusions and future prospects are drawn in Sec. 9.

[1] https://nugrid.github.io/

2 Nucleosynthesis processes

Different properties and conditions for the burning phases, that will be described in more detail in the present section, can be seen in Fig. 1.

	Fuel	Products: Main	Products: Secondary	T_c (GK)	ρ_c (g cm^{-3})	τ (yr)	$\mathcal{L}^*$ $L_\odot$	Processes
0.8–8 $M_\odot$	H	He	^{14}N	0.04	4.53	8×10^6	6.3×10^4	pp-chains CNO-cycles
	He	C, O	^{18}O, ^{22}Ne s-process	0.2	968	1.2×10^6	10^5	3α-reaction ^{12}C(α,γ)^{16}O s-process
≥8 $M_\odot$	C	Ne, Mg	Na	0.9	1.7×10^5	10^3	1.4×10^5	^{12}C+^{12}C
	Ne	O, Mg	Al, P	1.6	3.1×10^6	0.6	1.5×10^5	^{20}Ne(γ,α)^{16}O α+X…
	O	Si, S	Cl, Ar, K, Ca	2	5.6×10^6	1.25	1.5×10^5	^{16}O+^{16}O QSE
	Si	Fe	Ti, V, Cr, Mn, Co, Ni	3.3	4.3×10^7	11.5 days	1.5×10^5	^{28}Si+$\gamma \rightarrow$ n, p, α n+X, p+X, … QSE, NSE

Figure 1: Burning Phases of Stars: The Central Temperatures T_c, Central Densities ρ_c , Burning Timescales τ, and Luminosities $\mathcal{L}^*$ are for a 20 $M_\odot$ Star. Taken from [1, p. 277].

2.1 Hydrogen burning

For masses greater than $0{,}08 M_\odot$, hydrogen burning starts when the core temperature T_c reaches about 5×10^6 K [2, p. 119].

2.1.1 Proton-proton chain

$$4\ {}^1_1\mathrm{H}^+ \longrightarrow\ {}^4_2\mathrm{He}^{2+} +\ 2\ \mathrm{e}^- +\ 2\ \nu_\mathrm{e} +\ 26{,}731\ \mathrm{MeV} \tag{1}$$

The reaction sequence above is a representation of reactants and products of the pp-chain. The real sequence starts with the production of a deuteron.

$${}^1_1\mathrm{H}^+ +\ {}^1_1\mathrm{H}^+ \longrightarrow\ {}^2_1\mathrm{H}^+ +\ \mathrm{e}^+ +\ \nu_\mathrm{e} \tag{2}$$

This is followed by proton capture on the deuteron.

$$ {}^{2}_{1}\mathrm{H}^{+} + {}^{1}_{1}\mathrm{H}^{+} \longrightarrow {}^{3}_{2}\mathrm{He}^{2+} + \gamma \tag{3} $$

In analogy to chemical reactions, the binding energy released in a reaction is given by the reaction Q-value, which is defined as the difference in binding energy before and after the reaction, which includes the sum of the masses of all reaction partners before the reaction (in the entrance channel) and the sum of masses of final nuclei (in the exit channel).

$$ Q_{nuc} = B_{before} - B_{after} = \left[\left(\sum_{initial} m_{nuc}^{initial} \right) - \left(\sum_{final} m_{nuc}^{final} \right) \right] c^2 \tag{4} $$

The pp-reaction, as given in the Eqs. 2 and 3, has a reaction Q-value of Q_{nuc} = 0,42 MeV. The effective energy release, however, is 1,442 MeV because annihilating the positron with an electron from the plasma produces an additional 1,022 MeV [1, p. 277] in photons. After the production of ^{3}He, several reaction paths become possible. They are numbered as pp-I chain, pp-II chain, and so on.

The pp-I chain

$$ {}^{3}_{2}\mathrm{He} + {}^{3}_{2}\mathrm{He} \longrightarrow {}^{4}_{2}\mathrm{He} + 2\ {}^{1}_{1}\mathrm{H} \tag{5} $$

The total released energy after the chain completion is 26,732 MeV, but 2,2% of this energy (0,59 MeV) is lost to the production of neutrinos. The pp-I chain is dominant at temperatures ranging between 10 to 14 MK [1, p. 281].

The pp-IV (Hep) chain

$$ {}^{3}_{2}\mathrm{He} + {}^{1}_{1}\mathrm{H} \longrightarrow {}^{4}_{2}\mathrm{He} + \mathrm{e}^{+} + \nu_{\mathrm{e}} \tag{6} $$

The rate for this reaction is very low, and so far, no neutrinos from this reaction in the Sun have been detected. The total energy released is 18,8 MeV [1, p. 281].

2.1.2 Helium catalyzed chains

There are three reaction chains that transform hydrogen to helium but require the initial presence of helium or carbon to act as a catalyst.

The pp-II chain (Lithium burning)

$$ {}^{3}_{2}\mathrm{He} + {}^{4}_{2}\mathrm{He} \longrightarrow {}^{7}_{4}\mathrm{Be} + \gamma \tag{7} $$

$$^{7}_{4}\mathrm{Be} + \ \mathrm{e}^{-} \longrightarrow \ ^{7}_{3}\mathrm{Li} + \ \nu_{\mathrm{e}} \tag{8}$$

$$^{7}_{3}\mathrm{Li} + \ ^{1}_{1}\mathrm{H} \longrightarrow \ 2\ ^{4}_{2}\mathrm{He} \tag{9}$$

This chain is dominant at temperatures of 14 to 23 MK [1, p. 281].

90% of the neutrinos produced in the second reaction carry an energy of 0,861 MeV, while the remaining 10 percent carry 0,383 MeV. Neutrino energy depends on whether $^{7}_{3}\mathrm{Li}$ is produced in the ground or in an excited (metastable) state.

4% of energy is lost in the pp-II chain (one neutrino from the pp-reaction and one from the electron capture on $^{7}\mathrm{Be}$).

The pp-III chain

$$^{3}_{2}\mathrm{He} + \ ^{4}_{2}\mathrm{He} \longrightarrow \ ^{7}_{4}\mathrm{Be} + \ \gamma \tag{10}$$

$$^{7}_{4}\mathrm{Be} + \ ^{1}_{1}\mathrm{H} \longrightarrow \ ^{8}_{5}\mathrm{B} + \ \gamma \tag{11}$$

$$^{8}_{5}\mathrm{B} \longrightarrow \ ^{8}_{4}\mathrm{Be} + \ \mathrm{e}^{+} + \ \nu_{\mathrm{e}} \tag{12}$$

$$^{8}_{4}\mathrm{Be} \longrightarrow \ 2\ ^{4}_{2}\mathrm{Be} \tag{13}$$

The last three stages of the pp-III chain release 18,209 MeV, and the pp-III chain is dominant for temperatures above 23 MK [1, p. 281].

This chain does not produce much energy in the Sun. Its generation of very high energy neutrinos (up to 14,06 MeV) was significant for solving the solar neutrino problem.

28.3% of energy is lost in the pp-III chain (one neutrino from the pp-reaction and one from the decay of $^{8}\mathrm{B}$).

Different paths that can pp-chain take are shown in Fig. 2.

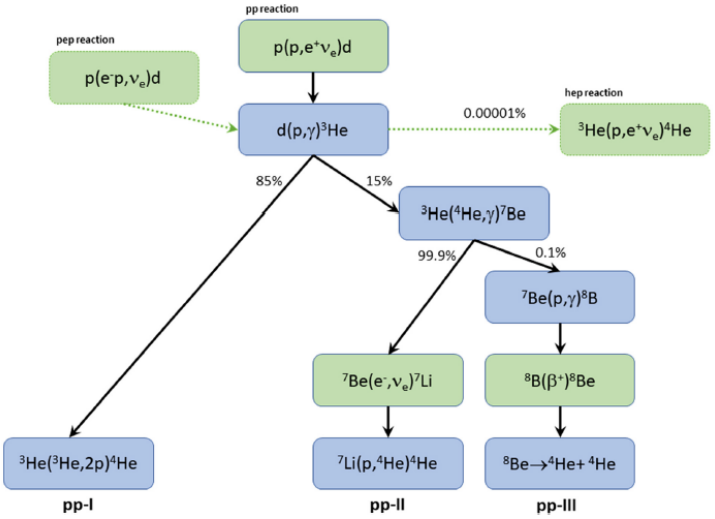

Figure 2: Diagram showing pp-I, pp-II, and pp-III chain. Taken from [1, p. 278].

2.1.3 CNO cycle

The carbon-catalyzed cycle is called the CNO cycle. Various paths and nuclei involved in the CNO cycles have the same net result.

$$4\ {}^{1}_{1}\mathrm{H} + \ 2\ \mathrm{e}^{-} \longrightarrow\ {}^{4}_{2}\mathrm{He} + \ 2\ \mathrm{e}^{+} + \ 2\ \mathrm{e}^{-} + \ 2\ \nu_{\mathrm{e}} + \ 3\ \gamma + \ 24{,}7\ \mathrm{MeV} \tag{14}$$

$$4\ {}^{1}_{1}\mathrm{H} + \ 2\ \mathrm{e}^{-} \longrightarrow\ {}^{4}_{2}\mathrm{He} + \ 2\ \nu_{\mathrm{e}} + \ 7\ \gamma + \ 26{,}7\ \mathrm{MeV} \tag{15}$$

Almost immediate annihilation of positrons with electrons releases energy in the form of γ rays.

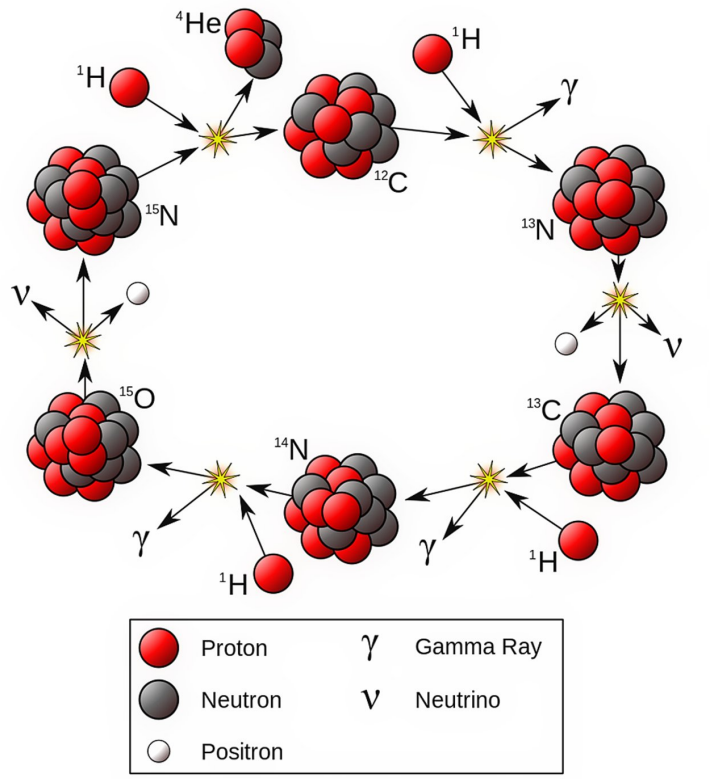

Figure 3: Visualization of the CNO-I cycle. Credit: Borb (`https://supernova.eso.org/exhibition/images/0418_cno-1080/`)

CNO-I:

$$^{12}_{6}\mathrm{C} \rightarrow\ ^{13}_{7}\mathrm{N} \rightarrow\ ^{13}_{6}\mathrm{C} \rightarrow\ ^{14}_{7}\mathrm{N} \rightarrow\ ^{15}_{8}\mathrm{O} \rightarrow\ ^{15}_{7}\mathrm{N} \rightarrow\ ^{12}_{6}\mathrm{C} \tag{16}$$

CNO-II:

$$^{15}_{7}\mathrm{N} \rightarrow\ ^{16}_{8}\mathrm{O} \rightarrow\ ^{17}_{9}\mathrm{F} \rightarrow\ ^{17}_{8}\mathrm{O} \rightarrow\ ^{14}_{7}\mathrm{N} \rightarrow\ ^{15}_{8}\mathrm{O} \rightarrow\ ^{15}_{7}\mathrm{N} \tag{17}$$

CNO-III:

$$^{17}_{8}\mathrm{O} \rightarrow\ ^{18}_{9}\mathrm{F} \rightarrow\ ^{18}_{8}\mathrm{O} \rightarrow\ ^{15}_{7}\mathrm{N} \rightarrow\ ^{16}_{8}\mathrm{O} \rightarrow\ ^{17}_{9}\mathrm{F} \rightarrow\ ^{17}_{8}\mathrm{O} \tag{18}$$

CNO-IV:

$$^{18}_{8}\mathrm{O} \rightarrow\ ^{19}_{9}\mathrm{F} \rightarrow\ ^{16}_{8}\mathrm{O} \rightarrow\ ^{17}_{9}\mathrm{F} \rightarrow\ ^{17}_{8}\mathrm{O} \rightarrow\ ^{18}_{9}\mathrm{F} \rightarrow\ ^{18}_{8}\mathrm{O} \tag{19}$$

In Fig. 3 it can be seen how ^{12}C, after a series of proton captures and β-decays, grows into the ^{15}N, and than after the final proton capture, ^{15}N with α-decay closes the CNO-I cycle by becoming ^{12}C again.

CNO-III and CNO-IV branches are only significant in massive stars.

Visualization of different forms of the CNO cycle is shown in Fig. 4.

There is the question of the origin of the $^{12}_{6}$C in protostars entirely made of primordial hydrogen and helium since there is no $^{12}_{6}$C. But once helium burning begins, this nucleus is produced.

The proton capture rate exceeds the β-decay rate in high temperatures and pressure found in novae and x-ray bursts. These CNO cycles are typically called hot CNO cycles due to very high-temperature conditions. Because of the β-decay rate, they are also called β-limited CNO cycles.

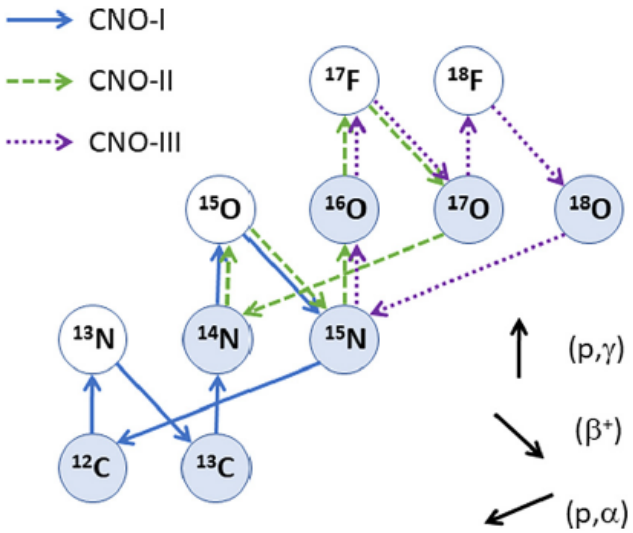

Figure 4: Diagram showing the CNO-I, CNO-II, and CNO-III cycles. Shaded circles indicate stable nuclides. The β^+-decays release a e^+ and a ν_e. Taken from [1, p. 282].

2.2 Helium burning

The next stage of nucleosynthesis is Helium burning. This requires a mass larger than $\sim 0{,}5 M_\odot$ and not only high temperatures of $(1-2) \times 10^8$ K [2,

p. 161-162] but also high densities of ($10^5 - 10^8$ kg m^{-3}) [1, p. 292].

$$\alpha + \ \alpha \longrightarrow \ {}^{8}_{4}\mathrm{Be} - 0{,}09 \text{ MeV} \tag{20}$$

$$\alpha + \ {}^{8}_{4}\mathrm{Be} \longrightarrow \ {}^{12}_{6}\mathrm{C} + \ 2\ \gamma + \ 7{,}37 \text{ MeV} \tag{21}$$

The total energy produced after completion of the helium-burning process is equal to $\sim$ 7,27 MeV [2, p. 162].

The helium accumulated in the core of lower mass stars on the red-giant branch is kept stable from further collapse by electron degeneracy pressure.

2.3 Heavier nuclei

Since the nucleosynthesis of elements depends on temperature and pressure, heavier nuclei can be combined only in environments with high temperatures and densities. Following nucleosynthesis reactions occur in the cores of massive stars with at least 8 $M_\odot$.

2.3.1 Carbon burning

Carbon burning requires temperatures greater than $(6 - 8) \times 10^8$ K and densities greater than 10^8 kg m^{-3} [1, p. 300].

$${}^{12}_{6}\mathrm{C} + \ {}^{12}_{6}\mathrm{C} \longrightarrow \ {}^{20}_{10}\mathrm{Ne} + {}^{4}_{2}\mathrm{He} + \ 4{,}52 \text{ MeV} \tag{22}$$

$${}^{12}_{6}\mathrm{C} + \ {}^{12}_{6}\mathrm{C} \longrightarrow \ {}^{23}_{11}\mathrm{Na} + {}^{1}_{1}\mathrm{H} + \ 2{,}24 \text{ MeV} \tag{23}$$

$${}^{12}_{6}\mathrm{C} + \ {}^{12}_{6}\mathrm{C} \longrightarrow \ {}^{23}_{12}\mathrm{Mg} + {}^{1}\mathrm{n} - \ 2{,}63 \text{ MeV} \tag{24}$$

2.3.2 Neon burning

Only stars with more than about 10 $M_\odot$ [1, p. 301] pass through neon-burning hydrostatically. Neon burning occurs in high temperatures (around $1{,}2 \times 10^9$ K) and densities (4×10^9 kg m^3).

$${}^{20}_{10}\mathrm{Ne} + \ \gamma \longrightarrow \ {}^{16}_{8}\mathrm{O} + {}^{4}_{2}\mathrm{He} \tag{25}$$

$${}^{20}_{10}\mathrm{Ne} + \ {}^{4}_{2}\mathrm{He} \longrightarrow \ {}^{24}_{12}\mathrm{Mg} + \gamma \tag{26}$$

2.3.3 Oxygen burning

Neon burning precedes oxygen burning. Oxygen ignites in the conditions of temperatures ranging between $1{,}5 \times 10^9$ and $2{,}6 \times 10^9$ K and in densities ranging between $2{,}6 \times 10^{12}$ and $6{,}7 \times 10^{12}$ kg m^{-3}.

$$^{16}_{8}\mathrm{O} + \ ^{16}_{8}\mathrm{O} \longrightarrow \ ^{28}_{14}\mathrm{Si} + ^{4}_{2}\mathrm{He} \tag{27}$$

$$^{16}_{8}\mathrm{O} + \ ^{16}_{8}\mathrm{O} \longrightarrow \ ^{31}_{15}\mathrm{P} + ^{1}_{1}\mathrm{H} \tag{28}$$

$$^{16}_{8}\mathrm{O} + \ ^{16}_{8}\mathrm{O} \longrightarrow \ ^{31}_{16}\mathrm{S} + \mathrm{n} \tag{29}$$

$$^{16}_{8}\mathrm{O} + \ ^{16}_{8}\mathrm{O} \longrightarrow \ ^{30}_{14}\mathrm{Si} + 2\ ^{1}_{1}\mathrm{H} \tag{30}$$

$$^{16}_{8}\mathrm{O} + \ ^{16}_{8}\mathrm{O} \longrightarrow \ ^{30}_{15}\mathrm{P} + ^{2}_{1}\mathrm{D} \tag{31}$$

2.3.4 Silicon burning

After completing the hydrogen, helium, carbon, neon, and oxygen burning phases, the silicon burning phase begins. It is the last phase of fusion for massive stars.

$$^{28}_{14}\mathrm{Si} + \ ^{4}_{2}\mathrm{He} \longrightarrow \ ^{32}_{16}\mathrm{S} \tag{32}$$

$$^{32}_{16}\mathrm{S} + \ ^{4}_{2}\mathrm{He} \longrightarrow \ ^{36}_{18}\mathrm{Ar} \tag{33}$$

$$^{36}_{18}\mathrm{Ar} + \ ^{4}_{2}\mathrm{He} \longrightarrow \ ^{40}_{20}\mathrm{Ca} \tag{34}$$

$$^{40}_{20}\mathrm{Ca} + \ ^{4}_{2}\mathrm{He} \longrightarrow \ ^{48}_{20}\mathrm{Cr} \tag{35}$$

$$^{48}_{20}\mathrm{Cr} + \ ^{4}_{2}\mathrm{He} \longrightarrow \ ^{52}_{26}\mathrm{Fe} \tag{36}$$

$$^{52}_{26}\mathrm{Fe} + \ ^{4}_{2}\mathrm{He} \longrightarrow \ ^{56}_{28}\mathrm{Ni} \tag{37}$$

As nuclei grow their size, the repulsion of the electric force against the new protons grows stronger. For the elements heavier than ^{56}Fe, electric force becomes so strong that energy needs to be added for further fusion to occur. ^{56}Fe has the most nuclear binding energy (minimal energy that is required to

disassemble the nucleus into its constituents), as shown in the Fig. 5, making it the most efficiently bound nucleus.

Due to the energy consumption for further fusion, when no more nuclei needed for the silicon burning are left in the star's core, no more processes can release enough energy to counteract gravity. In the beginning, gravitational contraction will heat the star's core (2,7–3,5 GK) and may explode in a Type II supernova.

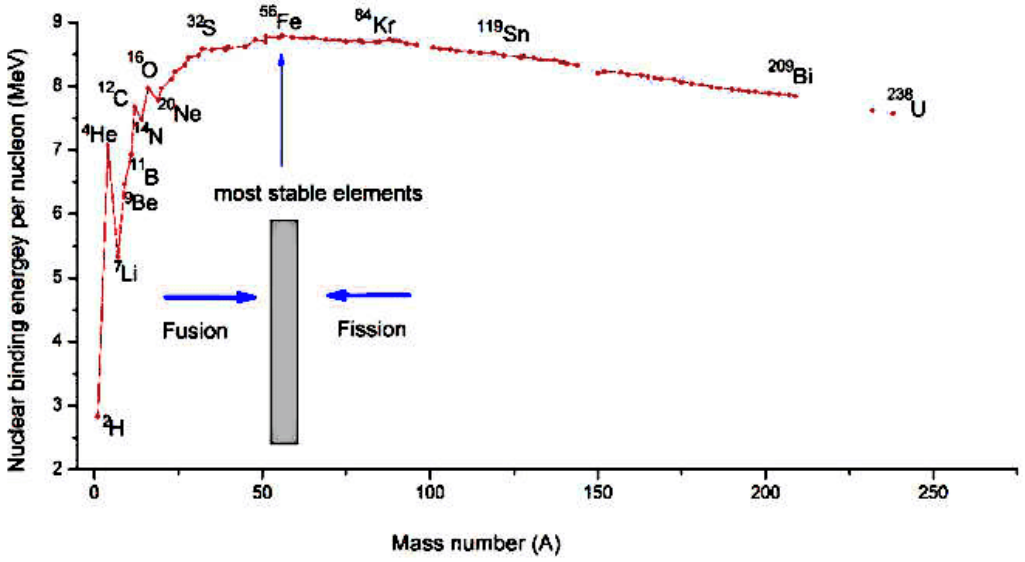

Figure 5: Dependence of negative binding energy per nucleon on the mass number. Taken from [3].

2.3.5 S-process

A Series of nuclear processes responsible for creating atomic nuclei heavier than iron is called the slow neutron capture process or s-process. Neutron capture is radiative and may be followed by β-decay.

$$(\mathrm{Z}, \mathrm{A}) + \ \mathrm{n} \longrightarrow \ (\mathrm{Z}, \mathrm{A}+1) + \text{one or more } \gamma - \text{rays} \tag{38}$$

$$(\mathrm{Z}, \mathrm{A}+1) \longrightarrow (\mathrm{Z}+1, \mathrm{A}+1) + \mathrm{e}^{-} + \nu_{\mathrm{e}} \tag{39}$$

For ω_n as the neutron capture rate and ω_β as the β-decay rate, each one being an average value over many nuclei in a given circumstance, two regimes may be defined:

1. $\omega_n << \omega_\beta$

2. $\omega_n >> \omega_\beta$

The first defines the s-process for slow neutron capture. The second one defines r-process, r for rapid.

2.3.6 R-process

In the rapid neutron capture process, r-process, multiple neutron capture occur before β-decay. Nuclei are shifted far from the line of stability (shown in the Fig. 6) to the neutron-rich regions. A nuclear drip line sets the boundary beyond which nuclei decay by a proton or neutron emission. A nuclear drip line prevents further neutron capture unless β^--decay occurs.

It is possible to identify nuclei that most likely have been created by the s-process or r-process among the stable nuclei. However, some nuclei cannot be created by either process.

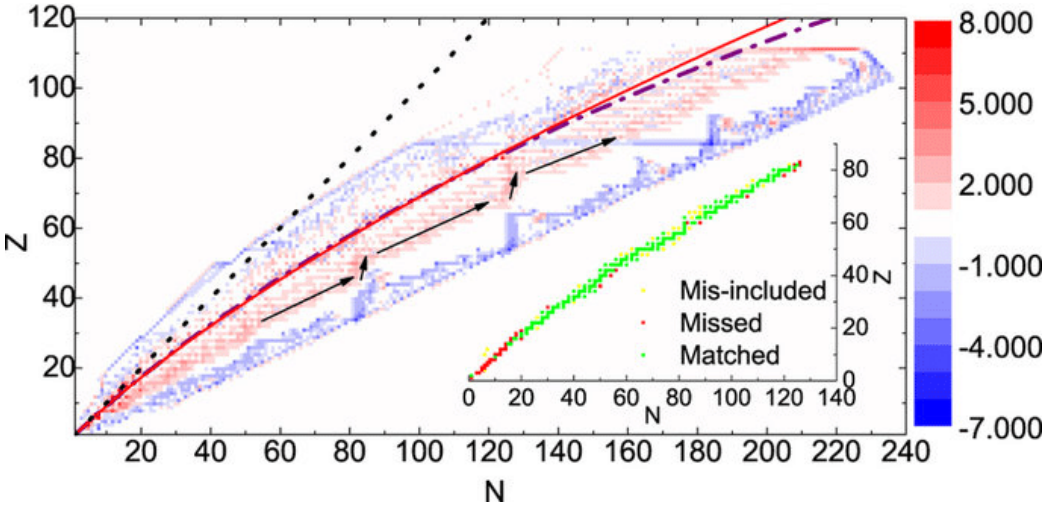

Figure 6: The solid red line and the purple dash-dotted line are empirical predictions of β-stability lines. The solid black lines with arrows could be able to outline the r-process. The black dotted line is auxiliary, following Z = N. The inset demonstrates the fitting result of the condition. Green dots are 192 stable nuclei that match the condition. Yellow dots are 31 unstable nuclei included by the condition. The red dots are 40 stable nuclei missed by the condition. The ratio of correct prediction is relatively high. Taken from [4].

2.3.7 P-process

Proton-rich nuclei (or p-nuclei, shown in Fig. 7) stand for neutron-deficient isotopes of the elements from selenium to mercury. The nucleosynthesis of elements heavier than iron is dominated by neutron capture processes. However, there are several proton-rich nuclei that neutron-capture processes cannot reach.

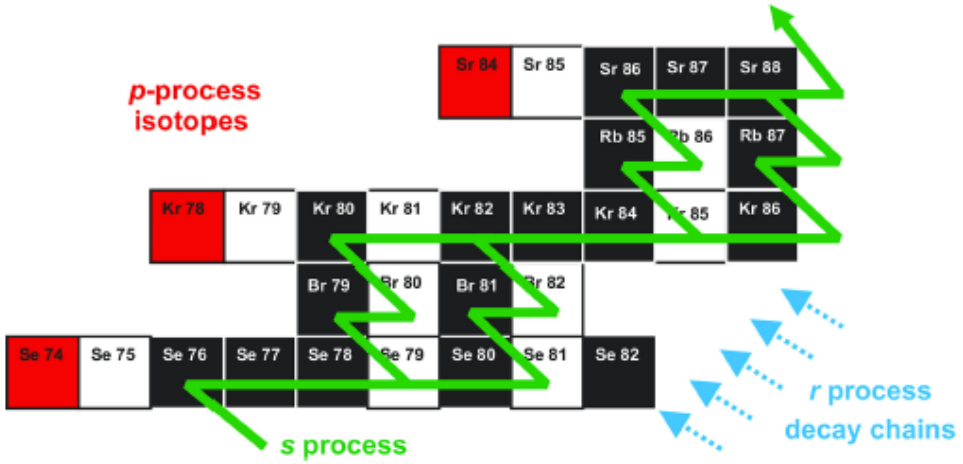

Figure 7: Diagram explaining s, r and p-process. Taken from [1, p. 330].

P-process is at least one nucleosynthesis process needed to produce the p-nuclei. In older literature, the p-process implies proton capture. Proton capture could be more efficient in producing p-nuclei, especially the heavier ones because the electric charge will increase with the addition of every proton. An increase in the electric charge will increase the repulsion of the next proton to be added. There are, at first, three possibilities for p-nuclei creation.

1. Proton capture on the stable isotope of the next lower element (Z-1).
2. By ejection of neutrons from isotopes of heavier elements.
3. By emission of protons and/or α-particles from isotopes of heavier elements.

As discussed before, 1. possibility, due to the increase of the Coulomb barrier, may only contribute to the creation of the lightest p-nuclei up to Ru, if at all.

2. and 3. possibilities are referred to as the γ-process. At sufficiently high plasma temperature and not too high density, neutrons, protons, and α-particles are ejected from a nucleus. This is a photodisintegration reaction which is the reverse of a capture reaction. It was first found in the outer layers of models of massive stars during their explosion in a core-collapse supernova but also in models of WD exploding as type Ia supernovae.

3 Primordial nucleosynthesis

The time at which the physics of complex nuclei began to play a role was when the Universe was about 9×10^8 K, and the density was about 2×10^4 kg m^{-3}: the Universe contained photons, neutrinos, and antineutrinos, electrons, and nucleons. The ratio of photons to neutrons to protons was $10^{11} : 13 : 87$, and there were enough electrons to neutralize the protons electrically. Those photons were the ones that will become the 2,7 K black body radiation after scattering, absorption and re-emission.

At $t = 225$ s, some initial nucleosynthesis took place. These primordial nucleosyntheses lasted only 30 minutes, during which lighter nuclei were produced (hydrogen, deuterium, lithium).

The nucleosynthesis that will produce heavier nuclei, as we can observe nowadays, will happen in stars. Hydrogen and helium are processed in the interior of stars during the several stages of stellar evolution. The matter in the Universe now is close to 24% helium and 76% hydrogen.
Information is taken from [5, p. 345-347].

4 Stellar evolution

4.1 Virial theorem

The life of stars begins with the cool cloud of interstellar material dominated by the presence of hydrogen and helium. These protostar contract gravitationally and heats up due to the virial theorem.

The virial theorem sets the relation between the total kinetic energy of a self-gravitating body and the gravitational potential energy.

$$2E_{kin} + Epot = 0 \tag{40}$$

Total energy $E = E_{kin} + Epot$ if the system is bound must be negative, and the binding energy $B = -E$.

$$dB = -d(\bar{E}_{kin} + \bar{E}_{pot}) = d\bar{E}_{kin} \tag{41}$$

At any time, the star has a secular equilibrium in which the gravitational forces are balanced by internal pressure. Thus an increase in binding energy is accompanied by an increase in E_{pot}, resulting in an increase in temperature. This means that protostar, as it contracts, the increasing binding energy has to be radiated from the surface.

$M_\odot$ unit is the mass of the Sun and is equal to $1{,}99 \times 10^{30}$ kg. Suppose electrons are in a box and fill all the energy levels up to the Fermi energy, further compression of the box results in a rise of Fermi energy and the total energy of the electrons. This is called electron degeneracy pressure.

Suppose the mass of our protostar is less than approximately $0{,}1M_\odot$. In that case, the contraction stops because the soup of electrons, protons, and α-particles at the center can support this weight by its electron degeneracy pressure.

4.2 Stars birth

As described, stars and their planets are formed from a collapsing molecular cloud. According to the virial theorem, collapsing cloud will heat up due to the release of the gravitational binding energy. In the early stages of collapse, the molecular cloud is optically thin, and the temperature increases only moderately. The collapse can then be approximated by free fall. When opacity increases due to the increase of density and ionization,

a strong increase in temperature begins. This object is called a protostar, and its luminosity is drawn from the gravitational binding energy release. Protostar evolutionary track on the HR diagram is called the Hayashi line, which runs almost vertically from high luminosity to higher temperature toward the main sequence.

When temperature and density in the center of the protostar reach the conditions required to ignite H-burning, the stars establish hydrodynamic equilibrium, implying that the contraction is halted and the luminosity and temperature remain at an almost constant level for as long as the nuclear reactions in the core can supply the energy lost through the surface. Therefore the ignition of nuclear burning does not effectively heat the star but prevents further contraction and thus precludes a further temperature increase! There is a brief halt in contraction even before the onset of H-burning. The interstellar medium contains a small amount of deuterium. It can be consumed by the reaction $p + d \rightarrow 3\ He$ already at a temperature much lower than the H-burning temperature (i.e., before $p + p \rightarrow d$ is possible). Therefore there is a short episode in the pre-main sequence (PMS) evolution of the star in which deuterium burning very briefly ($\lesssim$100 yr) prevents further contraction by establishing a quasi-hydrostatic equilibrium.

4.3 Stable nucleosynthesis stages

The minimal mass for igniting H-burning is about 0,08 $M_\odot$. Protostars below this mass limit never ignite H-burning and are stable because of the gas pressure. They are called brown dwarfs. Planets that are gas giants, such as Jupiter ($\approx$ 0,001 $M_\odot$) or Saturn ($\approx$ 0,0003 $M_\odot$), do not even ignite deuterium burning. This is one of several possible criteria to distinguish planets from brown dwarfs.

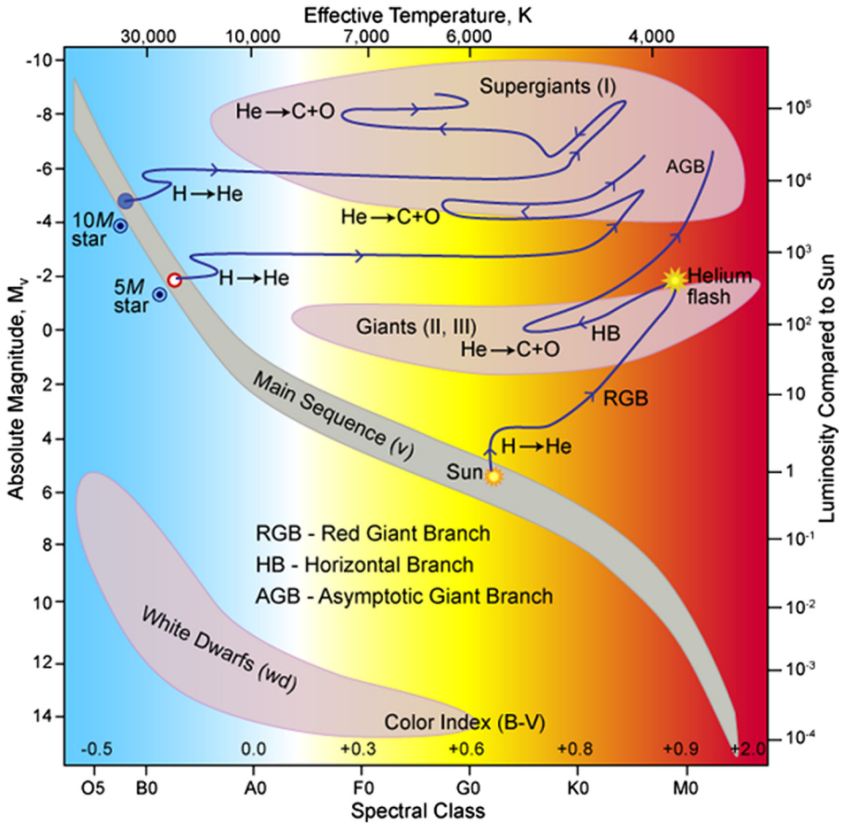

Figure 8: HR diagram shows the stages of the star's life. Taken from [1, p. 262].

After the ignition of helium burning, the helium-burning phase of the star's life begins. This is stable, and the longest faze. This is the faze of Main Sequence stars in the HR diagram (as shown in Fig. 8).

The next stages of a star's life depend on the mass of the star, shown in Table 1.

Mass Range ($M_\odot$)	**Final Stage**	**Remark**
$0{,}08 \lesssim M \lesssim (0{,}6 - 0{,}8)$	He WD	Only H-burning
$(0{,}6 - 0{,}8) \lesssim M \lesssim 2{,}3$	Planetary Nebula, C/O WD	H-burning, core He-flash
$2{,}3 \lesssim M \lesssim 8$	Planetary Nebula, C/O WD	H-burning, He-burning, AGB phase
$8 \lesssim M \lesssim 10$	ccSN, neutron star	Final burning phase under degenerate conditions during core collapse (e^--capture SN)
$10 \lesssim M \lesssim (20 - 25)?$	ccSN, neutron star	All burning phases under hydrostatic conditions
$(20 - 25)? \lesssim M \lesssim 130$	ccSN, black hole	All burning phases under hydrostatic conditions

Table 1: Final evolutionary stages of stars with non-zero metallicity as a function of initial mass. Taken from [1, p. 267].

4.4 Final stage

When a star finishes its burning phase by using up all the fuel left in the core, the gravitational force prevails the gas pressure, and the star starts collapsing. It will continue collapsing until it either starts the next burning phase or becomes stable under its own weight by non-degenerate or degenerate gas pressure. After the last burning phase is completed, the final outcome of a star mostly depends on the mass.

4.4.1 White dwarf

A WD is a stellar core remnant of stars with a mass below 8 $M_\odot$. In a WD, electron degeneracy pressure counteracts gravitational force keeping it stable. In these conditions, nuclei in plasma are stacked close to each other, making them highly dense. A WD has an average density of $\sim 10^6$ g cm^{-3}.

Their masses range from 0,3 $M_\odot$ to 1,2 $M_\odot$ with a distribution peak at 0,59 $M_\odot$ (taken from [6]). The maximum possible mass of the non-rotating and non-magnetized WD is about 1,4 $M_\odot$ [7] and is called the Chandrasekhar limit.

For stars with masses below $(0{,}6 - 0{,}8)$ $M_\odot$ there is only H-burning; WD is mainly composed of He. The star, during its collapse, barely ejects any mass shells.

Stars with mass grater than $(0{,}6 - 0{,}8)$ $M_\odot$ and lesser than 2,3 $M_\odot$ ignite He-burning, but it does not establish a stable He-burning phase called a core He-flash. A part of the core and the outer layers of the unburnt He and H are ejected, while the remnant of the core becomes a WD mainly composed of C and O.

Stars with mass grater than 2,3 $M_\odot$ and lesser than 8 $M_\odot$ achieve hydrodynamic equilibrium after ignition of He. In the He-burning phase, there is H-burning in a shell around a He core. Star moves from the main sequence to the red giant branch in the HR diagram and, later, to the asymptotic giant branch. After the He-burning phase ends, a short and unstable phase of He-shell flashes begins. In this phase, a star goes through pulses of rapid expansion and shrinking, ejecting shells of material. After the ejection of the remaining surface layers in a superwind, the phase of He-shell flashes ends. Remnant is a CO WD surrounded by a planetary nebula.

4.4.2 Supernova

As the stars with enough mass to complete all burning phases (from H- to Si-burning) reach the end of the Si-burning phase, their core becomes rich with Fe. Nucleosynthesis of Fe atoms will take away energy and not produce it as for lighter atoms. The core collapse will begin. The collapsing matter will reach high velocities, resulting in a rapid increase in temperature and density. This increase in temperature will blow off the star's outer layers in a dramatic explosion called a supernova.

4.4.3 Neutron star

For stars with masses above 8 and below $(20 - 25)$ $M_\odot$ remnant is a neutron star. In the formation process, protons and electrons combine to produce neutrons, making a neutron star almost completely composed of neutrons. Neutron degeneracy pressure keeps neutron stars from further gravitational

collapse.

Neutron stars with typicallly 1.4 $M_\odot$ and 10 km radius have an average density of about 10^{15} g cm^{-3} [1, p. 389], which is larger than nuclear ($\rho_0 = 2 \times 10^{14}$ g cm^{-3}) density by almost an order of magnitude. The mass of neutron star is at least 1,1 $M_\odot$ and at most 2,5 $M_\odot$ [8].

Beyond a mass of 2,5 $M_\odot$ it is taught that gravity will overcome repulsion of the strong force and neutron degeneracy pressure producing a black hole. The most massive neutron stars detected to date have masses of $1{,}97 \pm 0{,}04$ $M_\odot$ (PSR J1614-2230) and $2{,}14 \pm 0{,}1 M_\odot$ (PSR J0740+6620, with a radius of about 30 km) [1, p. 389], close to the theoretical limit. The smallest observed black hole is about 5 $M_\odot$ leaving room for theories of exotic stars, but none were found.

After shrinking to the neutron star radius to keep angular momentum, the Stellar core keeps increasing its rotational speed. Neutron stars are known to have rotation periods in the range of 1,4 ms - 30 s. They are also known for their extremely strong magnetic field that, on the surface, can range from 10^{15} G [9]. Electrons accelerate along the field lines on the magnetic poles that do not need to be aligned with the rotational axis. Accelerated electrons produce curvature radiation that is strongly polarized towards the plane of curvature. Electromagnetic radiation from these neutron stars can be observed in pulses aligned with their rotation periods, and these types of neutron stars are called pulsars.

4.4.4 Black holes

For stars with mass greater than $(20 - 25)$ $M_\odot$, its final gravitational collapse will produce a region of spacetime with gravity so strong that even electromagnetic radiation can not escape it. The boundary of no escape is called the event horizon.

A black hole has only 3 independent physical properties: mass, electric charge, and angular momentum. The size of a black hole, as determined by the radius of the event horizon (Schwarzschild radius), is proportional to the mass, M:

$$r_s = \frac{2GM}{c^2} \approx 2{,}95 \frac{M}{M_\odot} \text{ km} \tag{42}$$

5 Novae

5.1 Roche lobe

The Roche lobe (visualization shown in Fig. 9) is a region of space around a star in which material is bound to the same star. The radius of the Roche lobe can be calculated by

$$R_{Roche} = |\vec{r_1} - \vec{r_2}| \frac{0{,}49\ q_m^{2/3}}{0{,}6\ q_m^{2/3} + \ln(1 + q_m^{1/3})} \tag{43}$$

where q_m is the mass ratio of the two bodies.

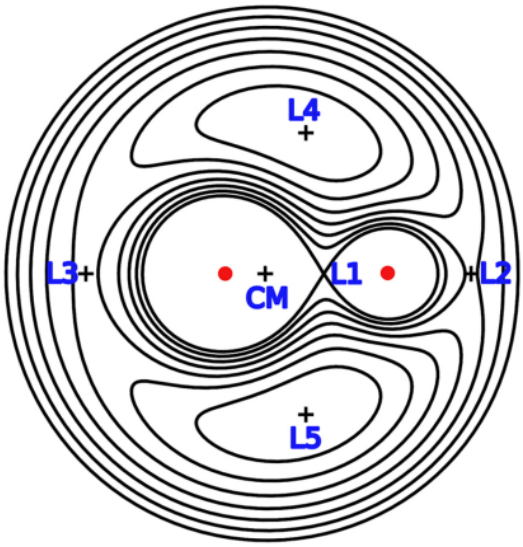

Figure 9: Roche lobe with Lagrange points. Taken from [1, p. 368].

Star that suddenly rose in luminosity carries the name nova (a new star). Every observed nova involves a WD in a close binary system. Three main sub-classes of novae are classical novae, recurrent novae, and dwarf novae.

5.2 Classical novae

Classical novae are the second-most frequent type of thermonuclear explosions observed in the Galaxy, with an estimated rate of 30 ± 10 yr^{-1} [1, p. 369] in the Galaxy.

As stars in a close binary system come closer, their Roche lobe shrinks. If the Roche lobe radius becomes smaller than the radius of the star, the transfer of matter from one star to its companion will begin. A WD accretes matter at a rate of $10^{-10} - 10^{-9}\ M_{\odot}\ \mathrm{yr}^{-1}$ [1, p. 369] from its companion star (main sequence, subgiant, or red giant).

The WD matter is degenerate, and the accreted hydrogen is compressed on the surface of the WD and also becoming degenerate. With more and more accreted matter, an increase in pressure, density, and temperature (by released gravitational binding energy) will ignite CNO cycles. Due to the degeneracy of the electron gas as the dominant pressure contribution, pressure cannot counteract the rising temperature giving rise to the release of energy by a thermonuclear runaway.

5.3 Recurrent novae

Recurrent novae are binary stars with two or more thermonuclear outbursts that have been registered. It is like classical nova, composed of a WD and either a main sequence, subgiant, or red giant star. The time interval between outbursts varies from 10 to 100 years, and it is proposed that classical novae will be seen as recurrent novae given enough time.

Table 2 shows 10 known recurrent novae in our galaxy.

Full name	Magnitude range	Known eruption years
CI Aquilae	8,6–16,3	2000, 1941, 1917
V394 Coronae Australis	7,2–19,7	1987, 1949
T Coronae Borealis	2,5–10,8	1946, 1866
IM Normae	8,5–18,5	2002, 1920
RS Ophiuchi	4,8–11	2021, 2006, 1985, 1967, 1958, 1933, 1907, 1898
V2487 Ophiuchi	9,5–17,5	1998, 1900
T Pyxidis	6,4–15,5	2011, 1967, 1944, 1920, 1902, 1890
V3890 Sagittarii	8,1–18,4	2019, 1990, 1962
U Scorpii	7,5–17,6	2022, 2010, 1999, 1987, 1979, 1936, 1917, 1906, 1863
V745 Scorpii	9,4–19,3	2014, 1989, 1937

Table 2: Ten known galactic recurrent novae. Taken from [10].

5.4 RS Ophiuchi

RS Ophiuchi (RS Oph) is a recurrent nova composed by a WD and a red giant. It is about 5000 light-years away in the constellation Ophiuchus.

The orbital period of RS Ophiuchi is 453,6 days, and the mass ratio $q = M_{WD}/M_{RG} = 0{,}59 \pm 0{,}05$. The WD mass is $M_{WD} = 1{,}2-1{,}4\ M_\odot$, and the red giant mass is $M_{RG} = 0{,}68-0{,}80\ M_\odot$. WD is close to the Chandrasekhar limit ($1{,}4\ M_\odot$), and is accreting material at the range $\sim (1-7) \times 10^{-7}\ M_\odot\ \mathrm{yr}^{-1}$. Typical gas temperature is around 10000–15000 K. This data on RS Ophiuchi

was taken from [11] and it or its approximations was used for the following simulations.

The latest outburst of RS Ophiuchi happened in August 2021. The starting of the outburst phase was observed by the Irish amateur astronomer [2]. In this occasion, the nova has been found emitting radiation in several energy bands, and, for the first time, in the very-high-energy (VHE, E >100 GeV) γ-ray band [12], [13].

[2] http://ooruri.kusastro.kyoto-u.ac.jp/mailarchive/vsnet-alert/26131

6 Tools and resources for the simulations

6.1 NuGrid

The Nucleosynthesis Grid (NuGrid) collaboration is an international collaboration that develops and maintains computational tools for nuclear astrophysics. NuGrid computational tools and programs are used for large-scale post-processing nucleosynthesis simulations with up-to-date and flexible nuclear physics input. Simulations are applied to complete sets of quiescent and explosive nuclear production environments. NuGrid has been active since the fall of 2007.

6.2 MESA software

MESA (Modules for Experiments in Stellar Astrophysics) is a collection of Fortran-95 modules for Experiments in Stellar Astrophysics. 1D stellar evolution simulations of almost any star can be made with the MESA star module. Other MESA modules provide stars with state-of-the-art numerical algorithms, e.g., for adaptive mesh refinement and time-step control, atmospheric boundary conditions, and modern input physics [opacities, equation of state (EOS), nuclear reaction rates, etc.].

6.3 NuGrid WENDI Astrohub

Astrohub is an implementation of the Cyber hubs: Virtual Research Environments for Astronomy system. Astrohub was developed by a team led by Falk Herwig in the Astronomy Research Centre. Cyber hubs allow multiple users to access the same virtual research environment composed of a combination of storage, processing capacity, and dedicated software packages specific to the particular research goals. Cyber hubs combine Docker virtualization with the latest JupyterHub notebook technology and incorporate third-party authentication. Astrohub link in reference: [14].

NuGrid WENDI is Astrohub with a collection of simulation tools as well as complete simulation frameworks that can be used by NuGrid members.

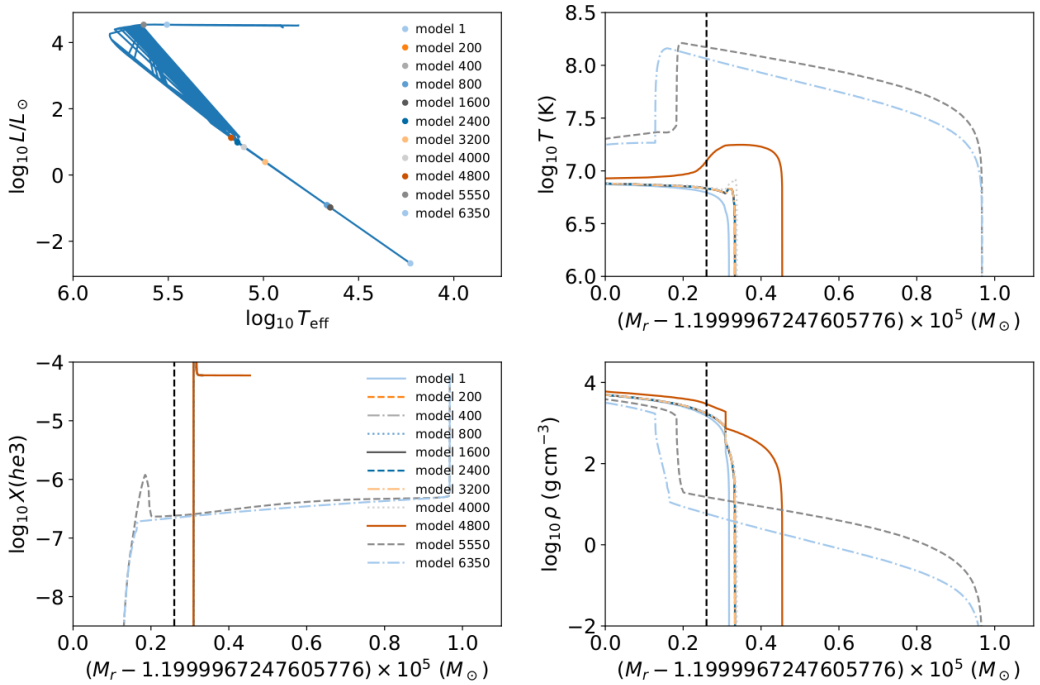

Figure 10: Top left: line of constant WD Roche lobe radius. Top right: temperature profiles of the accreted envelope. Bottom left: Abundance profile of ^{3}He. Bottom right: Density profile for different models.

7 Results

Following MESA simulations were done on NuGrid WENDI Astrohub with CaNPAN (The Canadian Nuclear Physics for Astrophysics Network) nova framework. Simulations were done on CO WD model with mass $M_{WD} =$ 1,2 $M_\odot$, core temperature $T_c = 10$ MK and accretion rate 6×10^{-8} $M_\odot$ yr^{-1}. In the nova framework were only 4 options for accretion rate; therefore, 6×10^{-8} $M_\odot$ yr^{-1} was chosen, which is the closest option to the accretion rate of RS Ophiuchi. Visualization of the results was done with Jupyter Notebook. Before plot generation, the mass of the red giant star and WD orbital period needed to be set. A mass of 0,74 $M_\odot$ and an orbital period of 10886 hours were the chosen values.
Two simulations were made with the difference of taking or not taking into account convective boundary mixing.
For simulation with convective boundary mixing, 6552 models were made. Figs. 10, 11, 12, and 13 show the results of the simulation.

For the simulation with no convective boundary mixing, 4786 models were

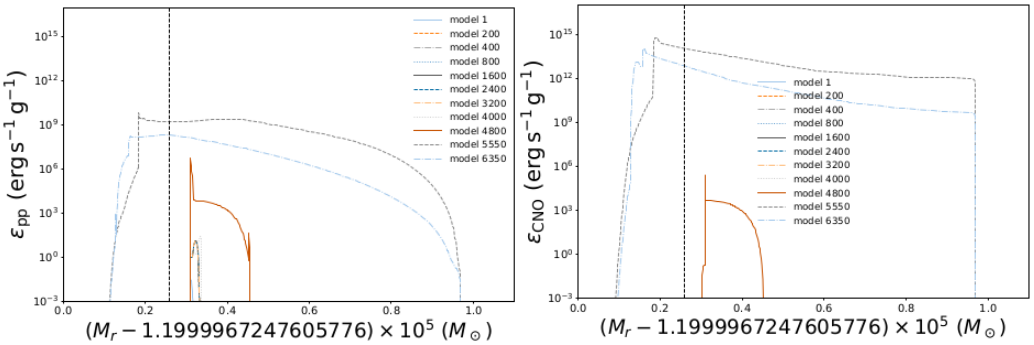

(a) Specific (per gram) energy production rates in pp chains.

(b) Specific (per gram) energy production rates in the CNO cycle.

Figure 11: Energy prodiction rates for pp chains and CNO cycles in the accreted envelope of the WD model with convective boundary mixing.

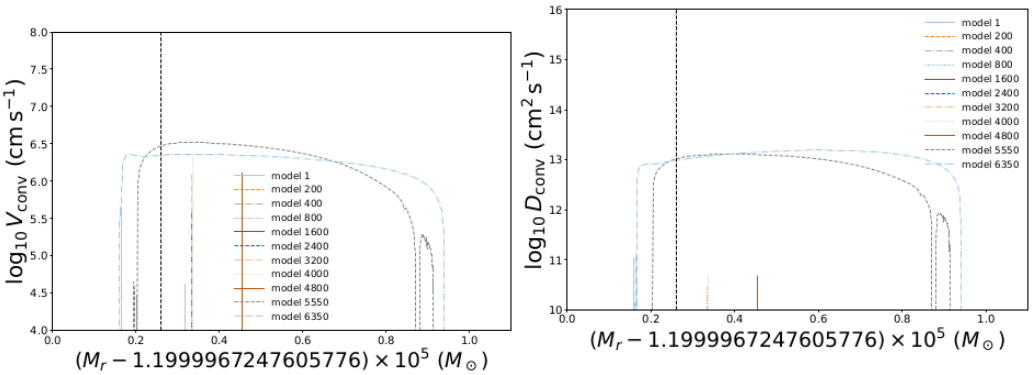

(a) Convective velocity (in m/s).

(b) Convective diffusion coefficient (in $cm^{2/s}$).

Figure 12: Convective velocity and convective diffusion coefficient in the accreted envelope of WD model with convective boundary mixing.

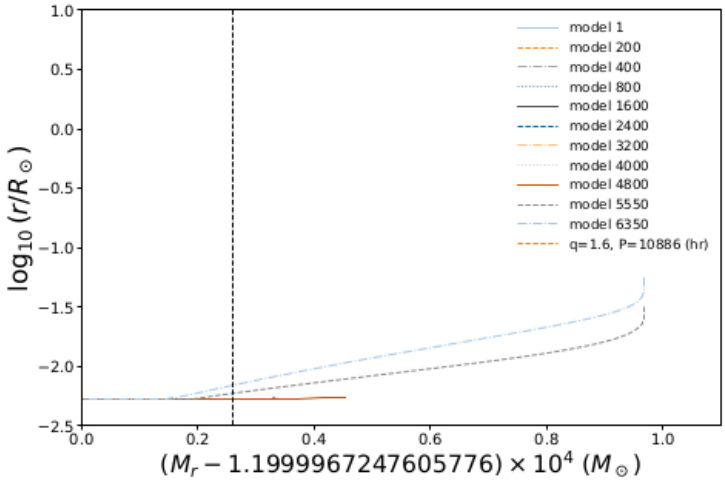

Figure 13: Radius profiles of different models.

made. Figs. 14, 15, and 16 show the results.

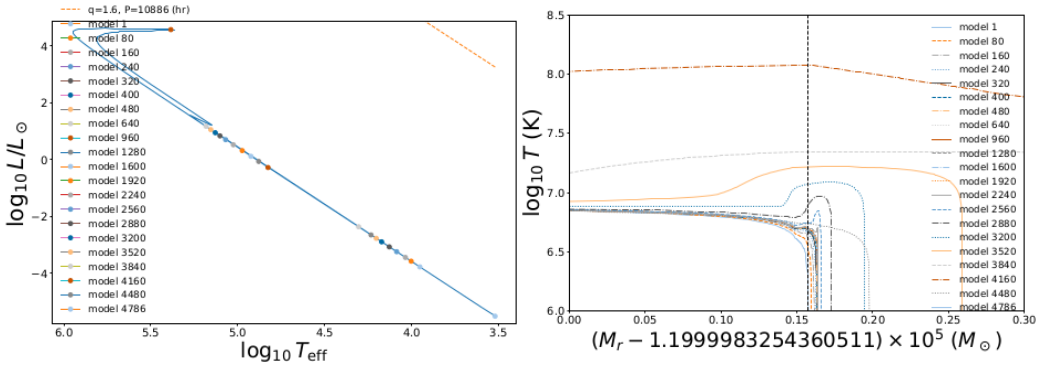

(a) Line of constant WD Roche lobe radius.

(b) Temperature profiles in selected models.

Figure 14: Line of constant WD Roche lobe radius and temperature profiles of the accreted envelope of the WD model without convective boundary mixing.

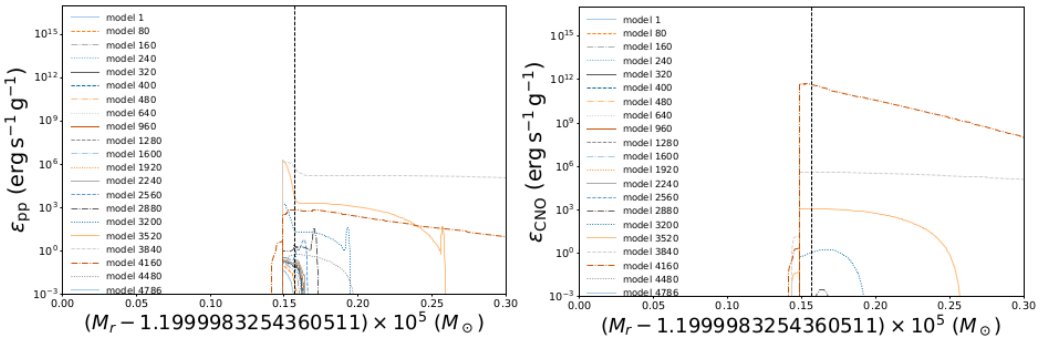

(a) Specific (per gram) energy production rates in pp chains.

(b) Specific (per gram) energy production rates in the CNO cycle.

Figure 15: Energy production rates in the pp chains and CNO cycle in the accreted envelope of the WD model without convective boundary mixing.

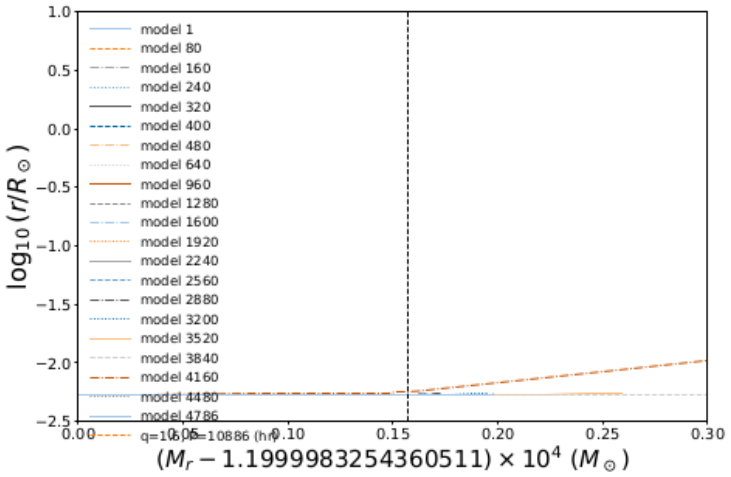

Figure 16: Radius profiles of different models.

8 Discussion

For the following discussion, the WD profile used for the first simulation (with convective boundary mixing) will be addressed as *Profile 1*, and the WD profile used in the second simulation (without convective boundary mixing) will be addressed as *Profile 2*.

Accreted envelope of the WD is very thin in mass ($\sim 1 \times 10^{-5} M_\odot$) relative to WD mass. In Figs. 10, 11, 12, 13, 14, 15, and 16, the zero point for the mass coordinate is the approximate mass coordinate of boundary between WD and accreted H-rich envelope. The mass difference is multiplied by 1×10^5 to zoom in on a thin envelope.

Model 5350 of *Profile 1* has the maximum temperature with $\log(T_{max}) =$ 8,2621, and the log density at T_{max} is 1,740. Model 4080 of *Profile 2* has the maximum temperature with $\log(T_{max}) = 8{,}2598$, and log density at T_{max} is 1,886. The vertical dashed black line marks the mass coordinate of the T_{max}.

The line of constant WD Roche lobe radius in the top left plot of Fig. 10 and Fig. 14a is calculated with the equation

$$r_L = \frac{0{,}49q^{2/3}}{0{,}6q^{2/3} + \ln(1 + q^{1/3})},\ 0 < q < \infty \tag{44}$$

and Kepler's law. It can be seen that these plots for *Profile 1* and *2* correspond with each other. It is because the Roche lobe radius depends only on

the distance between stars and their mass ratio, as seen in Eq. 43.

The top right plot in Fig. 10 and Fig. 14b are showing temperature profiles of the accreted envelope of *Profile 1* and *2*.

An evident rise of temperature for the same WD models of each profile can be seen at approximately the same mass coordinate where pp chains and CNO cycles start, as seen in Fig. 11 for the *Profile 1* and Fig. 15 for the *Profile 2*.

The fast drop of temperature can also be seen at the corresponding mass coordinate (the top right plot in Fig. 10 and Fig. 14b) as the ending of pp chains and CNO cycles (Fig. 11 and 15), which is the mass coordinate of the end of the accreted envelope.

The value 0 of the mass coordinate represents the approximate, not precise, mass coordinate of the boundary between WD and accreted H-rich envelope. Looking at the almost constant temperature at the beginning of the plots for temperature profiles (top right plot of Fig. 10 and Fig. 14b), it can be concluded that this is the temperature of the outer layer of the original WD.

The rise and the fall of the temperature, and the rise and the fall of the energy production rate of pp-chains and CNO cycles begins at the approximate mass coordinate of the boundary between WD and accreted H-rich envelope, and the end of the accreted envelope, respectively.

The difference between the models of the same profile is the mass coordinate of the end of accreted envelope. Simulations resulted with models that, in their evolution, started accreting material more and less recently and ended up with the same WD and red giant mass, WD core temperature, accretion rate, and orbital period. This gives various WD models with the difference in thickness of the accreted shells.

Looking at the Fig. 11 and Fig. 15 can be seen that there are much fewer models with ignited pp-chains and CNO cycles in *Profile 1* than in *Profile 2*. Mixing C and O from the WD with light elements from accreted envelope creates conditions where more mass in the accreted envelope is necessary for nucleosynthesis.

Using equations

$$M_{bol,1} - M_{bol,2} = -2{,}5 \log_{10} \frac{L_1}{L_2} \tag{45}$$

and

$$M = m + 5 - 5 \log_{10}(d_{pc}) = m + 5 - 5 \log_{10}(\frac{d_{light-years}}{3{,}2616}) \tag{46}$$

with RS Ophiuchi's apparent magnitude in the stable phase of 11, its approximate distance of 5000 light-years, and Sun's absolute magnitude $M_{bol,\odot}$ = 4,74, the logarithmic luminosity of RS Ophiuchi was calculated. It corresponds to:

$$\log_{10} \frac{L}{L_\odot} = 1{,}867$$

After comparing RS Ophiuchi logarithmic luminosity with the top left plot of Fig. 10 and Fig. 14a was concluded that a model between models 4800 and 5550 of *Profile 1* and a model between models 3840 and 4160 of *Profile 2* could be the best approximations of RS Ophiuchus. For both profiles model that best approximates should be among the models with the most accreted mass, which means that RS Ophiuchi has been accreting material for a long time. It is also among the models of both profiles that have both pp-chains and CNO cycles taking place in their accreted envelopes. This is necessary for models to have conditions for thermonuclear runaways, which confirms that these could be good models for nova RS Ophiuchi. Criteria for ruling out the existence or nonexistence of convective boundary mixing I did not find; therefore, both profiles will stay as possibilities for nova RS Ophiuchi.

9 Conclusions

Simulations of the nova RS Ophiuchi were made with MESA (Modules for Experiments in Stellar Astrophysics) star module as a part of the NuGrid (Nucleosynthesis Grid) collaboration's collection of software tools for simulations.
In the two different simulations that were made (for WD profiles with and without convective boundary mixing), various WD models were produced for different possibilities of the WD evolution. In Figs. 10, 11, 12, 13, 14, 15, and 16, where the simulations results are shown, some differences and similarities between the two different WD profiles can be noticed. Also, correlations between different properties of the same models for each WD profile can be seen, such as the correlation of the convective velocity and logarithmic density distributions of the WD profile with convective boundary mixing.
After calculating the logarithmic luminosity of the RS Ophiuchi, which resulted in $\log_{10} \frac{L}{L_\odot} = 1{,}867$, and comparing with the logarithmic luminosity of models in plots of constant WD Roche lobe radius, I concluded that RS Ophiuchi has a greater mass of the accreted envelope than most models. Models with logarithmic luminosity close to the one of RS Ophiuchi of both profiles have both pp-chain, and CNO cycles ignited in their accreted envelope, confirming that these models are good models of the nova RS Ophiuchi.
My goal was to make a nova simulation and learn from it, which was successfully done. But these results felt incomplete after I became acquainted with other computational tools. Therefore, for further research, I would suggest the following:

1. Running mppnp post-processing computations, which use results of the MESA nova simulations, are also available in the NuGrid Wendi Astrohub [14] for NuGrid members. These post-processing computations determine abundance profiles for multiple isotopes to understand the constitution of the WD better.

2. To create a self-consistent model for a complete cycle of recurrent novae as done in the article [15].

This model for the cycle of thermonuclear runaways and stable phases of the recurrent nova, the MESA nova simulations, and mppnp post-processing computations together would give a comprehensive picture of nova constitution and behavior.

Overall I am satisfied with the results of this thesis and very optimistic about the contribution of computational tools for research in physics, especially astrophysics.

References

[1] Rauscher, T. *Essentials of Nucleosynthesis and Theoretical Nuclear Astrophysics*. IOP Publishing Ltd 2020, 2020. doi: 10.1088/2514-3433/ab8737.

[2] Salaris, M. and Cassisi, S. *Evolution of Stars and Stellar Populations*. Wiley, 2005. ISBN 9780470092224. URL https://books.google.hr/books?id=p4ojTNkcFx8C.

[3] Girtan, M. et al. The Critical Raw Materials Issue between Scarcity, Supply Risk, and Unique Properties. *Materials*, 14(8):1826, April 2021. doi: 10.3390/ma14081826.

[4] Zhu, L. et al. Multilayer Network Analysis of Nuclear Reactions. *Scientific Reports*, 6:31882, August 2016. doi: 10.1038/srep31882.

[5] Williams, W. *Nuclear and particle physics*. Oxford at the Clarendon, 1991. URL https://books.google.hr/books?id=h10yMgEACAAJ.

[6] Fontaine, G., Brassard, P. and Bergeron, P. The potential of white dwarf cosmochronology1. *Publications of the Astronomical Society of the Pacific*, 113(782):409, apr 2001. doi: 10.1086/319535. URL https://dx.doi.org/10.1086/319535.

[7] Kalita, S., Mukhopadhyay, B. and Govindarajan, T.R. Significantly super-chandrasekhar mass-limit of white dwarfs in noncommutative geometry. *International Journal of Modern Physics D*, 30(05):2150034, mar 2021. doi: 10.1142/s0218271821500346. URL https://doi.org/10.1142%2Fs0218271821500346.

[8] Astashenok, A. et al. Causal limit of neutron star maximum mass in f(r) gravity in view of gw190814. *Physics Letters B*, 816:136222, 2021. ISSN 0370-2693. doi: https://doi.org/10.1016/j.physletb.2021.136222. URL https://www.sciencedirect.com/science/article/pii/S0370269321001623.

[9] Ferrario, L. and Wickramasinghe, D.T. Magnetic fields and rotation in white dwarfs and neutron stars. *Monthly Notices of the Royal Astronomical Society*, 356(2):615–620, 01 2005. ISSN 0035-8711. doi: 10.1111/j.1365-2966.2004.08474.x. URL https://doi.org/10.1111/j.1365-2966.2004.08474.x.

[10] Schaefer, B.E. COMPREHENSIVE PHOTOMETRIC HISTORIES OF ALL KNOWN GALACTIC RECURRENT NOVAE. *The Astrophysical Journal Supplement Series*, 187(2):275–373, mar 2010. doi: 10.1088/0067-0049/187/2/275. URL https://iopscience.iop.org/article/10.1088/0067-0049/187/2/275.

[11] Mikołajewska, J. and Shara, M.M. The massive co white dwarf in the symbiotic recurrent nova rs ophiuchi. *The Astrophysical Journal*, 847 (2):99, sep 2017. doi: 10.3847/1538-4357/aa87b6. URL https://dx.doi.org/10.3847/1538-4357/aa87b6.

[12] Acciari, V.A. Proton acceleration in thermonuclear nova explosions revealed by gamma rays. *Nature Astronomy*, 6:689–697, April et. al., 2022. doi: 10.1038/s41550-022-01640-z.

[13] H. E. S. S. Collaboration et al. Time-resolved hadronic particle acceleration in the recurrent nova RS Ophiuchi. *Science*, 376(6588):77–80, April 2022. doi: 10.1126/science.abn0567.

[14] Herwig, F. Astrohub, 2014. URL https://astrohub.uvic.ca/.

[15] Kato, M., Saio, H. and Hachisu, I. A self-consistent model for a full cycle of recurrent novae—wind mass-loss rate and x-ray luminosity. *The Astrophysical Journal*, 838(2):153, apr 2017. doi: 10.3847/1538-4357/838/2/153. URL https://dx.doi.org/10.3847/1538-4357/838/2/153.